Journal of Sol-Gel Science and Technology
https://doi.org/10.1007/s10971-018-4665-3

ORIGINAL PAPER: SOL-GEL AND HYBRID MATERIALS FOR DIELECTRIC, ELECTRONIC, MAGNETIC AND FERROELECTRIC APPLICATIONS

Ni^{2+}-substituted Mg–Cu–Zn ferrites: a colloidal approach of tuning structural and electromagnetic properties

L. M. Thorat[1] · J. Y. Patil[2] · D. Y. Nadargi[3] · U. R. Ghodake[3] · R. C. Kambale[4] · S. S. Suryavanshi[2]

Received: 8 December 2017 / Accepted: 16 April 2018

Abstract

A robust synthesis approach to Ni^{2+}-substituted $Mg_{0.25-x}Ni_xCu_{0.25}Zn_{0.5}Fe_2O_4$ ($0 \le x \le 0.25$ mol.) ferrimagnetic oxides using citrate assisted sol–gel process is reported. The route utilizes simple metal nitrate precursors in aqueous solution, thus eliminating the need for organometallic precursors. Citric acid acts as a fuel for the combustion reaction and forms stable complexes with metal ions preventing the precipitation of hydroxilated compounds to yield the composite ferrite structure by auto-combustion process. The XRD signatures, especially (3 1 1) plane, confirmed the formation of spinel structure. The linear growth of lattice constant from 8.385 to 8.409 Å was observed by Ni^{2+} substitution from 0 to 0.25. The dense microstructure is observed with the average grain size of 0.42–2.18 μm. The transport properties revealed the semiconducting behavior of as-prepared ferrite material, with an increase in the DC-electrical resistivity by the incorporation of nickel. The magnetic properties viz. initial permeability (μ_i) and magnetic moment (n_B) are explained, based on the deviation in saturation magnetization (M_s), anisotropy constant (K_1), density values, and exchange interactions. Furthermore, the effect of adding Ni^{2+} on the Curie temperature, frequency-dependent dielectric properties of the ferrite material are also discussed.

Electronic supplementary material The online version of this article (https://doi.org/10.1007/s10971-018-4665-3) contains supplementary material, which is available to authorized users.

✉ S. S. Suryavanshi
sssuryavanshi@rediffmail.com

[1] Department of Electronics, S. M. Dnyandeo Mohekar Mahavidyalaya, Kalamb 413507, Maharashtra, India

[2] School of Physical Sciences, Solapur University, Kegaon, Solapur 413255, Maharashtra, India

[3] Department of Electronics, Shri Shivaji Mahavidyalaya, Barshi, Solapur 413401, Maharashtra, India

[4] Department of Physics, Savitribai Phule Pune University, Pune 411007, Maharashtra, India

Published online: 11 May 2018

Graphical Abstract

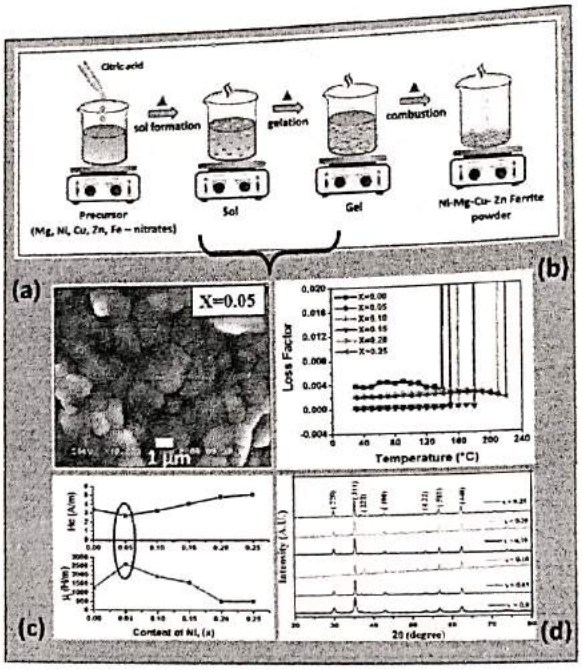

Keywords Mg-Ni-Cu-Zn ferrite · Citrate-gel method · Structural morphology · Spinel phase · Electrical resistivity · Initial permeability

Highlights

- A traditional and robust synthesis approach (citrate assisted sol-gel process) is adopted to develop Ni^{2+} substituted MgCuZn ferrimagnetic oxides.
- A detailed study of citrate autocombustion process, associated sol-gel reactions, and thereby structural and electromagnetic properties is made
- The addition of nickel results in increased aggregation of the colloidal backbone of ferrite and the loss of the mesoporous network structure.
- With increasing Ni content, an increase in the activation energy upto x = 0.10), decrease in loss tangent and saturation magnetization, are observed.

1 Introduction

Electronic devices perform a wide variety of tasks to make our lives more comfortable. Though their list is too long, to name few—mobile phones, i-pads/notepads, and entertainment gadgets are the most widely used electronic devices in today's life. The dynamic growth and development occurring in the field of telecommunication and information technology has emerged the need of electronic devices with smaller size, cost effective, and higher efficiency. Spinel ferrites (especially ferrimagnetic oxides) have key role in the technological applications, because of their interesting electrical, magnetic, and dielectric properties. Their high electrical resistivity, low eddy current, dielectric losses, high saturation magnetization, high permeability, high Curie temperature, good chemical stability, and mechanical hardness make them useful in many applications such as rod antennas, electronic devices, sensors, memory devices, data storage, and telecommunication [1–5]. Moreover, they have a niche market in equipment for medical diagnostics, microwave devices, gas sensors, information storage systems, and MultiLayer Chip Inductors (MLCIs) [6–9]. Mg–Cu–Zn ferrite is an appropriate magnetic material suitable for high frequency applications, due to its high resistivity ($>10^{11}$ Ω cm), high curie temperature (~500 K), and environmental stability [10–14].

In the state of the art, Hameed et al. [15] reported $ZnFe_2O_4$ and $Mg_xCu_{0.2}Zn_{0.82-x}Fe_{1.98}O_4$ (where $x = 0.20$, 0.25, 0.30, 0.35, and 0.40) nanoparticles for lithium storage. The sol–gel-assisted combustion route was employed to

develop the material. The application of nickel zinc ferrite and graphene nanocomposite as a modifier for fabrication of a sensitive electrochemical sensor for the determination of omeprazole in real samples is reported by Abbas et al. [16]. Similarly, Satalkar et al. reported role of cationic distribution in determining magnetic properties of $Zn_{0.7-x}Ni_xMg_{0.2}Cu_{0.1}Fe_2O_4$ nanoferrite. Zero values of Yafet–Kittel angle (α_{Y-K}) recommended the presence of Neel-type magnetic ordering in the developed ferrite [17]. For MLCI application, Kamble et al. discussed Mg–Cu–Zn ferrite ($Mg_{0.48}Cu_{0.12}Zn_{0.40}Fe_2O_4$) by ceramic and self-sustaining auto-combustion (sucrose) methods. The ferrite material using ceramic route was developed using required oxides in the powder form, whereas, aqueous metal nitrates along with sucrose as fuel were used in auto-combustion route for developing the identical ferrite material [18]. High magnetic loss Mg–Cu ferrites prepared by a solid-state reaction for ultrahigh frequency EMI suppression application, was investigated by Li et al. [19]. Mg–Cu–Zn ferrites are useful in the fabrication of multilayer chip inductor components as surface mount devices (SMD) for miniaturized electronic products such as cellular phone, digital diaries, videos camera recorders, etc. This system is particularly used in the SMD and MLCI due to their high electric resistivity and excellent soft magnetic properties at high frequencies. In view of it, as Ni^{2+} has higher magnetic moment (2.83 μB), compared to Mg^{2+} (2.00 μB), the magnetic properties with incorporation of Ni^{2+} in place of Mg^{2+} will be enhanced. In miniaturization of a device for MLCI applications, high μ_i, M_s, low eddy currents losses, and high electrical resistivity, which are important requisites, are almost complementary in the Ni-based ferrite [20].

Therefore, in the present work, attempts were made to develop Ni^{2+}-substituted Mg–Cu–Zn ferrite ($Mg_{0.25-x}Ni_xCu_{0.25}Zn_{0.5}Fe_2O_4$ ($0 \le x \le 0.25$)), using citrate assisted sol–gel, auto-combustion process, and investigate their structural and electromagnetic properties.

2 Experimental details

The general approach of making Ni^{2+}-substituted Mg–Cu–Zn ferrites involves following two major steps: (i) synthesis of material powder by sol–gel combustion and formation of pellets and/or toroids, (ii) investigation/characterization of the developed ferrite material.

2.1 Synthesis of ferrite material

In a typical synthesis, AR grade nitrates (magnesium nitrate ($Mg(NO_3)_2{\cdot}6H_2O$)), nickel nitrate ($Ni(NO_3)_2{\cdot}6H_2O$), copper nitrate ($Cu(NO_3)_2{\cdot}6H_2O$), zinc nitrate ($Zn(NO_3)_2{\cdot}4H_2O$), ferric nitrate ($Fe(NO_3)_3{\cdot}9H_2O$), and citric acid ($C_6H_8O_7$) were obtained from Sigma Aldrich and were used as received. The stoichiometry of the redox mixture for combustion was calculated and kept constant, based on total oxidizing and reducing valence of oxidizer and reductant (3:5 mol). The synthetic reagents were well mixed in the suitable amount of distilled water. The reaction mixture/sol was stirred for ample time, till it attained the homogeneous phase. The temperature of sol was eventually raised up to 425 K. In accordance with the natural behavior (Fig. 1: graph part), at the set temperature the sol viscosity increased gradually with respect to time. The highly viscous sol attained the percolation threshold and ended-up to a gel, enriched with water. The resultant gel was continued to heat treat at higher temperature (450–575 K). The viscous gel began frothing and eventually after water evaporation, the gel started exhausting into fast flameless auto-combustion reaction with the evolution of large amount of gaseous products after which it gets auto ignited. The obtained powder was calcinated in air at temperature 775 K for 2 h to remove the traces of unreacted leftovers, and retained the pure ferrite material. This powder was then made into pellets (15 mm diameter and 2 mm thickness) and toroids (Inner diameter = 1.5 cm, outer diameter = 2.5 cm, average height = 0.3 cm) with manual pressing machine (pressure

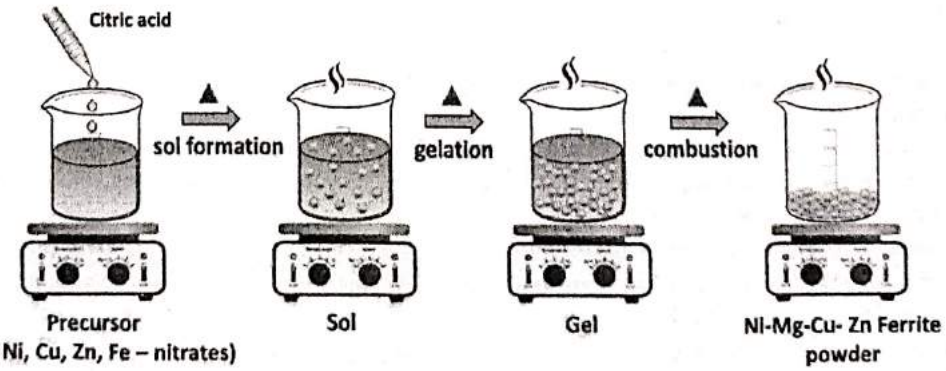

Fig. 1 Schematic illustration for the preparation of ferrite gel, using citrate initiated sol–gel process, along with reaction mechanism

= 1.5 ton/cm^2, binder: PVA). Finally, both pellets and toroids were sintered at 975 K for 2 h in air.

2.2 Characterizations of the material

Crystallinity and phase identification of ferrite was investigated using X-ray diffraction (XRD) by using Bruker D8 advanced X-ray diffractometer, SAED, EDS analysis. The structural analysis was done using both the electron microscopy techniques—SEM (Model 6306A JEOL-JSM, Japan) and TEM (Philips CM 200 FEG). The material was studied for its magnetic and inductance measurements using VSM (Lake Shore 7410 VSM) and controlled impedance analyzer (Hioki Model 3532–50 LCR HiTester, Japan), respectively. The frequency dispersion of initial permeability was studied in frequency range 100 Hz–1 MHz at 300 K. The initial permeability was determined from inductance measurements of coils using the formula [21]:

$$\mu_i = \frac{L}{0.0046N^2 h \log\frac{d_2}{d_1}}, \quad (1)$$

where, N = No. of copper turns on the toroid, h = thickness of toroid (cm), d_1, d_2 are inner and outer diameters, L = series inductance in (micro Henry).

LCR-Q meter (HP-4284A) was used to study the dielectric measurements at room temperature. The susceptibility measurements were carried out on powder sample using double coil set up [22]. The average crystallite size (t) was calculated from the Scherrer equation. The X-ray density ρ_x of the ferrite samples was calculated using the relation $\rho_x = 8\,M/Na^3$, where M is the molecular weight, N is the Avogadro's number (6.023×10^{23} atom/mol.), a^3 is the volume of the unit cell. The bulk density of the samples was estimated by Archimedes principle using xylene medium. $\rho_m = (w\rho')/(w - w')$, where w is the weight of sample in air, w' is the weight of sample in xylene, ρ' is the density of xylene. By means of temperature variations of susceptibility and initial permeability curves, the Curie temperature of the material was determined. DC-electrical resistivity measurement was carried out from room temperature to 500 °C using two probe methods.

2.3 Mechanism of citric acid initiated sol–gel chemistry

The citrate gel method is a traditional, simple sol–gel process, which offers the homogenous sol formation, and hence the final material. The impact of the homogeneity of citrate sol–gel precursors is on the reaction temperature, since the final crystalline metal oxide may be formed at considerably lower temperatures than powder solid-state methods where mass transport between grains limits the reaction [23]. Moreover, in the present approach, due to its better dispersion and versatility, the synthesis of multicomponent mixed ferrite materials can be better realized [24]. As the citric acid is widely used acidulent to form a gel, the viscosity of the precursor solution/sol shoots up with increasing temperature by the addition of citric acid, and the gel state is achieved. This gel is further heat treated to auto-combustion process, to yield the required ferrite material (Fig. 1.).

The stepwise progress and concerned reaction mechanism of the above process is explained as follows.

(i) Dissolution of metal salts in water:

In this first step, the precursors (metal nitrates) are added to the polar solvent (water), and subjected to the salvation process. Here, the salvation process can be referred to as hydration, as water is the solvent. The water molecules replace NO_3 ions, and get attached with the metal-cations. The formed aquo-cations are represented in the following reaction Eq. (2).

$$M(NO_3)_n + n(H_2O) \overset{solvation}{\rightarrow} [M(H_2O)_n]^{z+} + z(NO_3)^-, \quad (2)$$

where, $M(NO_3)n$ are the metal nitrates, and $[M(H_2O)_n]^{z+}$ are aquo-cations.

(ii) Complexation and chemically controlled condensation in the presence of the citric acid:

In the second step, under the control condition, citric acid is added to above solution containing aquo-cations. After addition of citric acid, it forms complex with hydrated metal ion, as per the following Eq. (3).

$$[M(H_2O)_n]^{z+} + z(NO_3)^- + x[C_6H_5O_7]^{z-} \rightarrow [M(C_6H_5O_7)_x(H_2O)_{n-x}]^{z-x}[(NO_3)_z^-(H_2O)_x]. \quad (3)$$

(iii) Formation of metal-citric acid chelates:

In third step, the stability of complex is further enhanced by getting converted into metal-citric acid chelate. Here, a metal ion gets attached with different carboxylate groups of citric acid, forming a cyclic chelate, which is a stable complex. The reaction scheme of forming stable chelate is shown in the following Eq. (4).

$$\begin{aligned} &[M(C_6H_5O_7)_x\,(H_2O)_{n-x}]^{z-x}\;[(NO_3)_z^-\,(H_2O)_x] + \\ &[M(C_6H_5O_7)_x\,(H_2O)_{n-x}]^{z-x}\;[(NO_3)_z^-\,(H_2O)_x] \\ &\downarrow \\ &\{[M(C_6H_5O_7)_{2x}\;\;(H_2O)_{n-2x}]\,[(NO_3)^-]_{2z}\,(H_2O)_{2x}\} \end{aligned} \quad (4)$$

3 Results and discussion

3.1 Crystallographic identification and density measurements

The crystal structure of as-developed ferrite was confirmed by grazing incidence XRD. Figure 2a shows the XRD

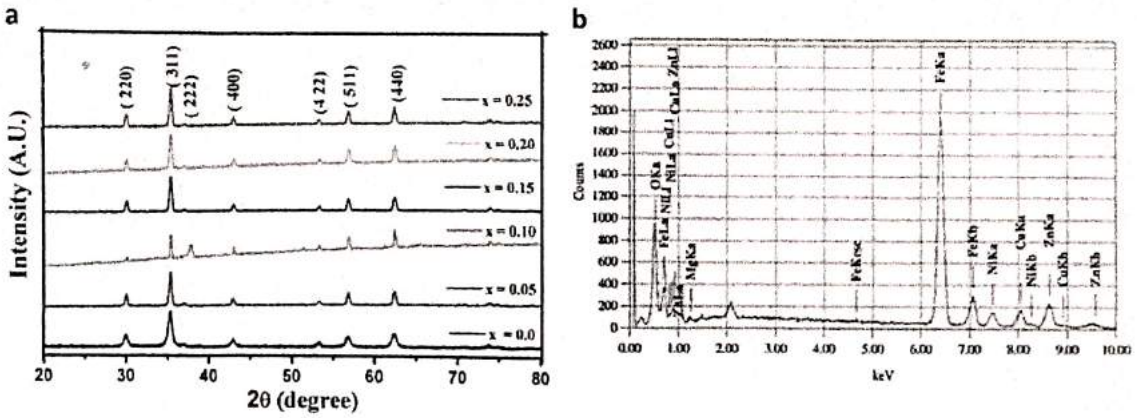

Fig. 2 **a** X-ray diffraction patterns of the $Mg_{0.25-x}Ni_xCu_{0.25}Zn_{0.5}Fe_2O_4$ ($0 \le x \le 0.25$) ferrites, **b** typical EDAX spectra for $Mg_{0.05}Ni_{0.20}Cu_{0.25}Zn_{0.5}Fe_2O_4$

Table 1 Data on lattice constant (a), crystallite size (t), bulk density (ρ_m), X-ray density (ρ_x), relative density (ρ_R), grain size (D), particle size (t_1) from TEM, activation energy, Curie temperature from DC resistivity (T_C) of $Mg_{0.25-x}Ni_xCu_{0.25}Zn_{0.5}Fe_2O_4$ ferrites

#	Content of Ni (x)	Lattice constant, a (Å)	Crystallite size,[a] t (nm)	Grain size,[b] D (μm)	Particle size (t_1)[c] (nm)	Activation energy (eV)		T_C from DC resistivity (°C)	Density		
						Ferri region	Para region		Bulk, ρ_m (g/cm^3)	X-ray, ρ_x (g/cm^3)	Relative, ρ_R (%)
1	0	8.385	51	0.42	315	0.46	0.67	151	4.35	5.18	84
2	0.05	8.392	48	2.18	237	0.50	0.74	153	5.05	5.21	97
3	0.10	8.400	51	1.22	201	0.63	0.87	171	4.91	5.23	94
4	0.15	8.405	47	1.36	338	0.46	0.70	184	4.89	5.26	93
5	0.20	8.407	49	2.01	180	0.49	0.73	201	4.82	5.30	91
6	0.25	8.409	53	1.45	114	0.59	0.83	227	4.90	5.33	92

[a]From XRD

[b]From SEM

[c]From TEM

patterns of different compositions of $Mg_{0.25-x}Ni_xCu_{0.25}Zn_{0.5}Fe_2O_4$ ($0 \le x \le 0.25$) ferrites. As expected, the material shows the exact same Bragg reflection signatures which are typical for the cubic spinel structure (highest intense peak corresponding to (3 1 1) plane). The relative intensities of the various reflections arising from the various crystal plane reflections are in well agreement with the standard JCPDS data # 08–0234, and exhibit the single-phase structure. The lattice constant (a) for all the compositions is tabulated in Table 1, which displays a gradual increase of "a" value with increasing Ni doping. As Ni^{2+} has larger ionic radii (0.78 Å) than Mg^{2+} (0.71 Å) ions, so when substitution of Ni^{2+} ions at the expense of Mg^{2+} ions takes place in the composition, the "a" value is expected to be reformed accordingly [25, 26]. The concentration of Cu^{2+} and Zn^{2+} ions are unchanged. Moreover, as the substitution of Ni^{2+} by Mg^{2+} takes place, the expansion of the unit cell is also expected to happen [27].

The crystallite size of the material is obtained using the Scherrer equation, which values between 47 and 53 nm. The values of density (relative density, observed density by X-ray, bulk density) and porosity are also listed in Table 1. All the ferrite samples exhibited high relative density (more than 90%) due to the presence of Cu in the ferrite system. Cu ions have a major role in the densification of the ferrite due to their high atomic mobility [28, 29]. The replacement of Mg atoms by Ni atoms, directs the increment in the relative density, due to their respective atomic mass. Magnesium has lower atomic mass (24.30 amu) than nickel (58.69 amu). Therefore, the relative density of the control sample ($x = 0.00$) was found lower (84%) as compared with the sample $x = 0.25$. It was also observed that the X-ray density of each sample was higher than the corresponding bulk density, due to the existence of the pores in the material after sintering treatment [30].

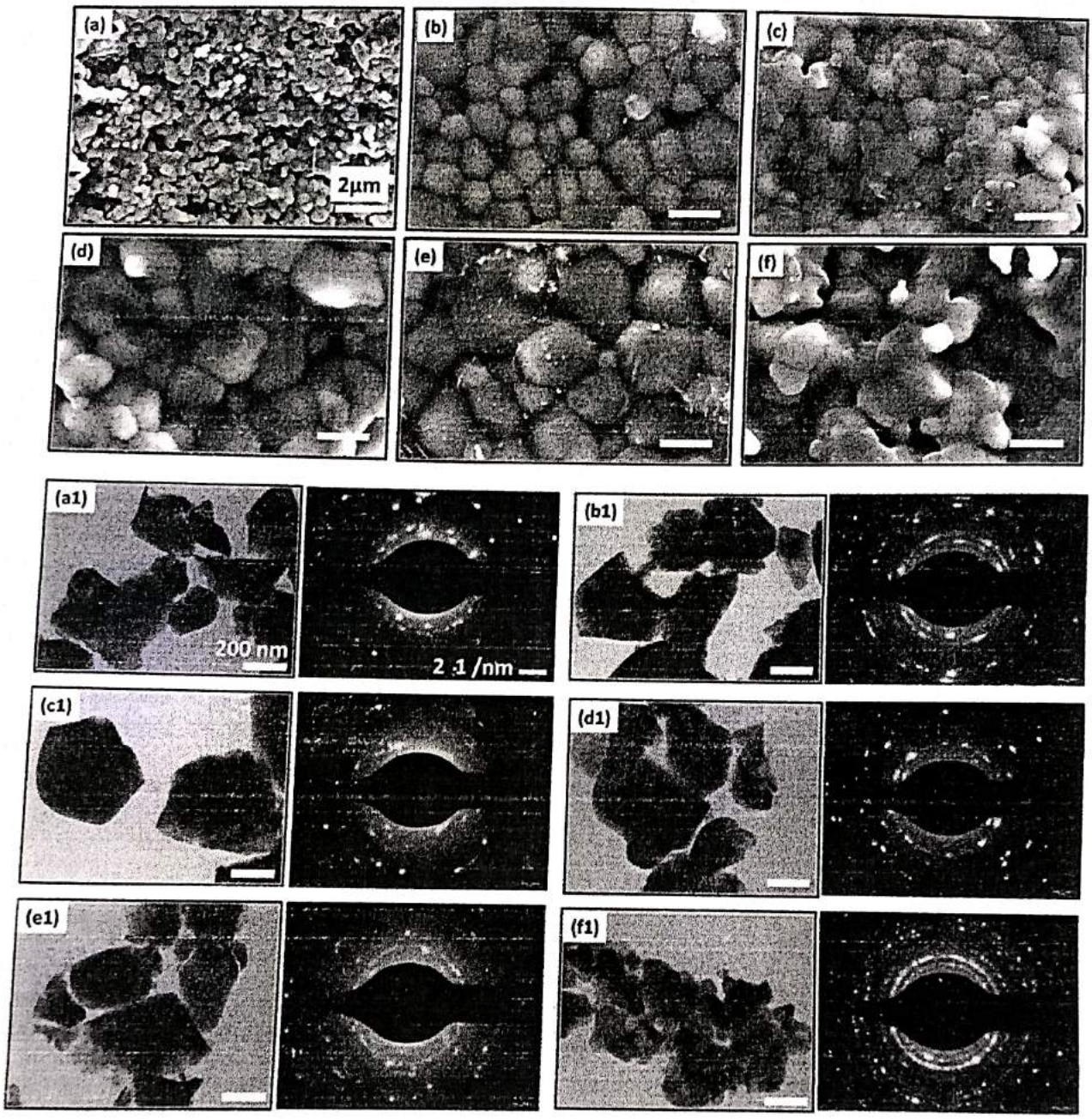

Fig. 3 **a–e** SEM images, and **a1–e1** TEM images with SAED pattern of $Mg_{0.25-x}Ni_xCu_{0.25}Zn_{0.5}Fe_2O_4$ ($0 \le x \le 0.25$) ferrites

3.2 Surface morphological properties

The typical pore diameter of a given MgCuZn ferrites is on the order of 100–300 nm depending on its density [31]. This mesoporous structure is seen in morphological analysis. SEM and TEM images of the pristine MgCuZn ferrite are shown in Fig. 3a and a1. The addition of nickel results in increased aggregation of the colloidal backbone of ferrite and the loss of the mesoporous network structure. During the sol–gel process, the mixed ferrite developed in the form of micron-sized secondary aggregation of pristine colloidal particles. The size of these aggregates is influenced by the nickel content in the sol. With increasing doping concentration, these aggregates are increasing in size (Fig. 3b–f, b1–f1). In addition, the volume fraction of nanoparticle-like nickel oxide-rich inclusions also increases with Ni content as seen qualitatively in the TEM images (higher contrast due to heavier element Ni in the bright field image).

Undoubtedly, the presence of copper also strongly affects the microstructure of the developed composite

Table 2 Elemental composition obtained from EDAX data for ferrites

#	Element	Atomic percentage of as-prepared ferrite					
		$X=0$	$X=0.05$	$X=0.10$	$X=0.15$	$X=0.20$	$X=0.25$
1	Mg^{2+}	4.28	3.65	2.64	1.79	0.97	—
2	Ni^{2+}	—	0.96	1.97	2.91	3.71	4.51
3	Cu^{2+}	4.10	4.43	4.67	4.45	4.77	4.39
4	Zn^{2+}	8.24	8.77	8.31	8.54	8.88	8.08
5	Fe^{3+}	33.47	36.56	34.63	35.97	37.59	35.99
6	O^{2-}	49.91	45.63	47.78	46.34	44.08	47.03

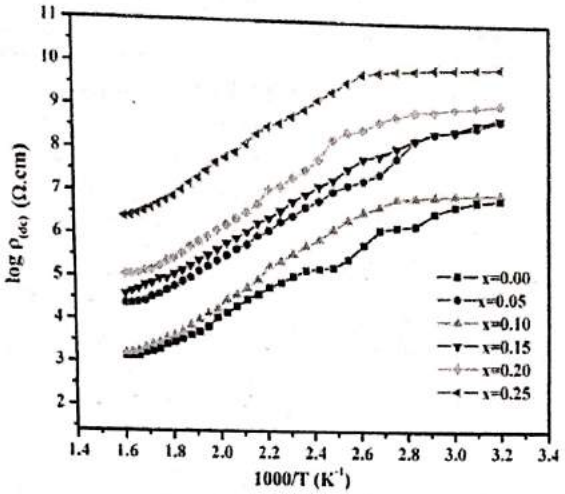

Fig. 4 DC resistivity (log ρ_{dc}) as a function of temperature (1000/T) for all the ferrites

ferrite. Cu facilitates the liquid phase sintering and increases the rates of cation inter diffusion because of its segregation to the grain boundaries [32]. If the driving force of grain boundary movement on each grain is homogeneous then uniform distribution of the grain size is expected. In contrast, if the driving force is non-homogenous then there is an abnormal grain growth [33]. The non-uniformity of the grain size in the present case can be attributed to the non-homogeneous driving force on the grains by liquid phase sintering [34]. The maximum particle size (338 nm) was observed for sample with $x=0.15$. Elemental analysis (EDS, Fig. 2b) of as-developed ferrite confirmed the presence of Ni, Mg, Cu, Fe, and O, and thereby the formation of Ni–Cu–Zn–Mg Fe_2O_4 (Table 2). The presence of circular bright spots/ring structure (Fig. 3, SAED patterns) corresponding to various planes as represented in XRD pattern, re-confirms the spinel structure of developed ferrite.

3.3 Transport property

Figure 4 shows the variation of DC-electrical resistivity of ferrites as a function of temperature. The material showed semiconducting nature, as rise in the temperature led to decrease its resistivity. The activation energies for different regions and the Curie temperature values are listed in Table 1. The activation energy was strongly influenced by Ni-addition and the type of conduction mechanism. The activation energy values for paramagnetic region are higher than those found in ferromagnetic region. This in turn indicates that the conduction in ferrites is due to hopping of polarons [35]. The conduction mechanism in ferrites can be explained based on Verwey principle, where different temperature regions arises due to conduction and hoping of extrinsic type carriers as well polarons. The change in slopes of two regions separated by Curie point evidenced the influence of the ferrimagnetic ordering on the conductivity process. This increase in DC resistivity due to Ni doping, is attributed to decrease in electron hopping at B site which is mainly responsible for conduction mechanism in ferrites [23, 24].

3.4 Dielectric properties

Dielectric constant (ε') as a function of frequency (100 Hz to 1 MHz) at room temperature for the ferrites is shown in Fig. 5a. Dielectric constant of all the ferrites decreased quickly with an increase in the frequency, and finally attained a constant value at higher frequencies. Such tendency in the dielectric measurement indicates the ferromagnetic behavior of the material [36]. Further, the dielectric properties are mainly governed by the conduction mechanism in the ferrites, where an electron hopping takes place.

In addition, complex dielectric constant (ε'') was investigated as a function of frequency depicted in Fig. 5b. It displayed the decrease in ε'' value with increase in the frequency, and after particular frequency, it responded independently against the frequency. This behavior is due to the existence of Maxwell–Wagner interfacial polarization, which exists in the inhomogeneous dielectrics [32, 33]. The large values of dielectric constants at low frequencies were observed due to the predominance of Fe^{2+} ions, interfacial dislocations, oxygen vacancies, and grain boundary defects [37].

Figure 5c shows the behavior of dielectric loss tangent of ferrites as a function of frequency (100 Hz to 1 MHz) at

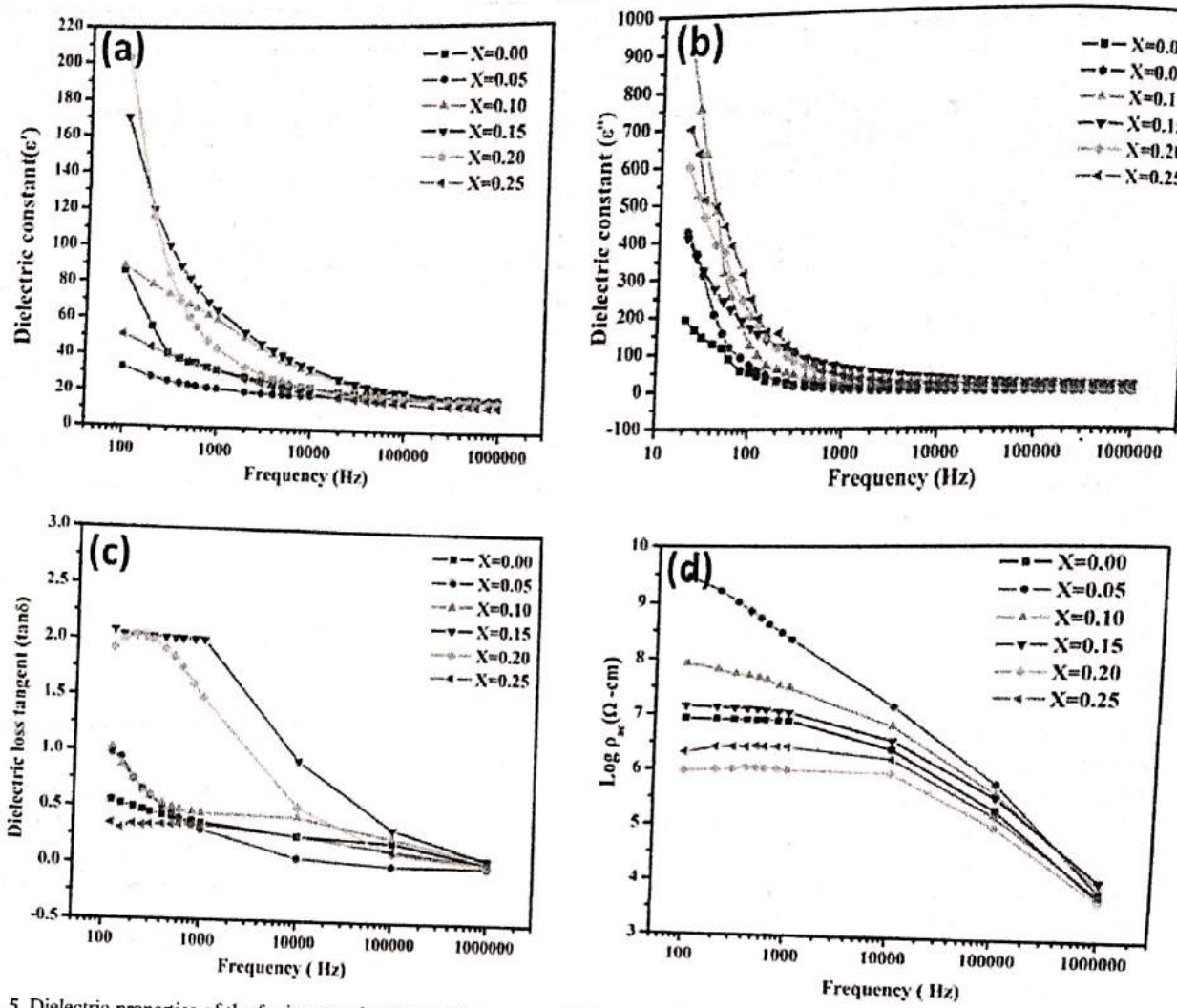

Fig. 5 Dielectric properties of the ferrites as a function of frequency. **a** Dielectric constant, ε', **b** complex dielectric constant, ε'', **c** dielectric loss tangent, tanδ, **d** AC resistivity, ρ_{AC}

room temperature. Around 100 kHz, the dielectric loss tangent got decreased, then-after remained constant at higher frequencies. This initial decrease of dielectric loss tangent can be explained based on phenomenological model. The dielectric losses in ferrites are generally reflected in the resistivity, i.e., materials with low resistivity exhibit high dielectric loss and vice versa. The decrease of loss tangent with increasing Ni^{2+} content is due to the exchange of electrons between Fe^{2+} and Fe^{3+}, which is responsible for the conduction mechanism in ferrites.

The AC resistivity of ferrites provide primary information related to the localization of charge carriers at grain/grain boundaries, intergranular tunneling of charge carriers across the grain boundary, and dielectric polarization of magnetic ions [38]. The AC resistivity of all the ferrite samples is depicted in Fig. 5d. It shows the room temperature AC resistivity of ferrites was found to be influenced by Ni addition. The maximum AC resistivity was observed for sample with $x = 0.05$. The ferrite samples with high density retained high AC resistivity. Furthermore, by the application of higher Ni, the probability of electron jumping through Fe^{2+}/Fe^{3+} led to reduction in the resistivity.

3.5 Magnetic properties

3.5.1 AC susceptibility studies

The normalized AC susceptibility (χ_T/χ_{RT}) of the ferrites as a function of temperature is depicted in Fig. 6a. The (χ_T/χ_{RT}) values of all the ferrites unhampered up to certain temperature, and thereafter they got decreased abruptly near the Curie temperature. The constant behavior of normalized susceptibility up to Curie temperature is because of insufficient thermal energy to disturb the aligned moments of spins. This behavior confirms the ferrimagnetic nature of

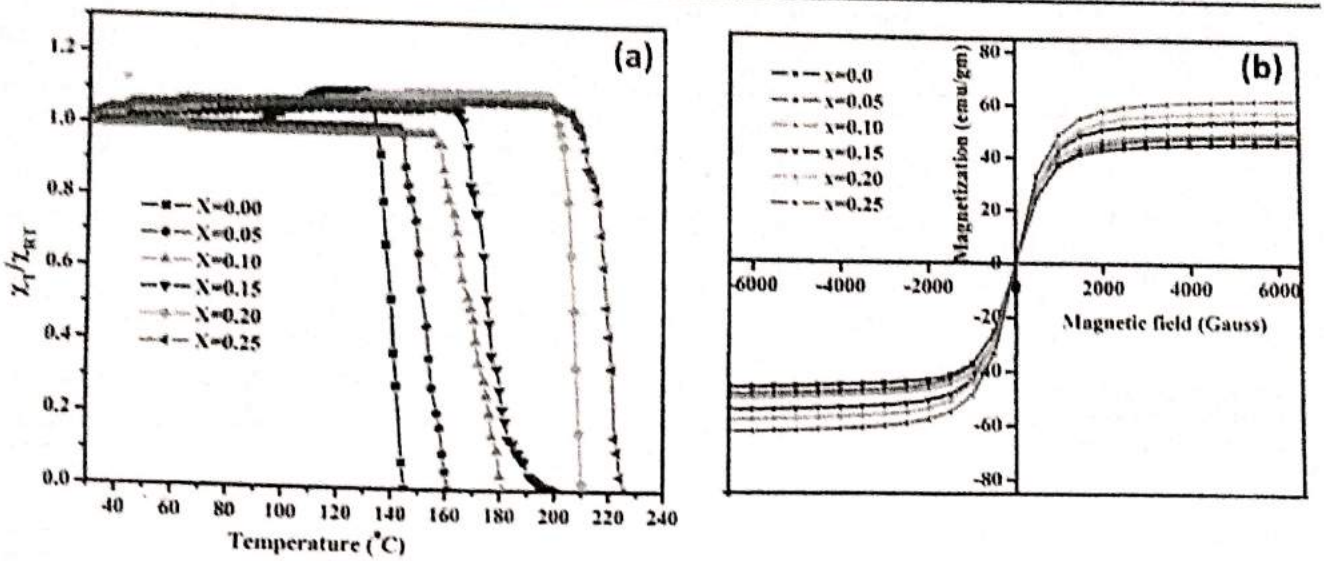

Fig. 6 Magnetic properties of the ferrites. a Normalized AC susceptibility (χ_T/χ_{RT}) as a function of temperature, b magnetic hysteresis loops

the material. However, above the Curie temperature the decrease in susceptibility is due to the sufficient thermal energy that disturbed the moment's alignment. Here, it indicates the transition of the material from ferrimagnetic to paramagnetic state.

The Curie temperature (DC resistivity) of all the ferrite samples is given in Table 1. The Curie temperature was found to increase with an increase in the nickel content, due to an increase in the ferrimagnetic region and at the same time, decrease in paramagnetic region. The Curie temperature of $NiFe_2O_4$ (585 °C) is higher as compared to $MgFe_2O_4$ (440°C). Also, the substitution of Ni causes the increase in A–B interactions resulting from replacement of Mg^{2+} by Ni^{2+} on octahedral (B) site, similar type of behavior was also observed in earlier studies [34, 35]. Above the Curie temperature a complete disordered state as well as the magnetization destruction is obtained. The high Curie temperature for $x = 0.25$ ferrite, is due to the strong exchange interaction (A–B) between the different sublattices [38].

3.5.2 Magnetization

The typical hysteresis loops of as-prepared ferrites at room temperature are shown in Fig. 6b. The magnetic hysteresis of all the samples exhibited a typical shape, confirming magnetic ordering the material. The values of saturation magnetization (M_s), coercivity and remanence for all ferrite compositions are given in Table 3. The saturation magnetization was increased with increasing Ni doping. This is can be explained based on cation distribution and the exchange interactions between A and B sites of the ferrite. In Mg–Cu–Zn ferrite, the stable Zn^{2+} ions occupy the A sites, whereas Ni^{2+} and Mg^2 ions occupies B sites. Ni^{2+} ions have higher magnetic moment (2.83 μ_B) than Mg^{2+} ions (2 μ_B). Therefore, it leads to an increase of the saturation magnetization of the ferrite [39]. The ferrite with $x = 0.25$ exhibited maximum value of saturation magnetization.

Table 4 gives the probable cation distribution, experimental, and theoretical magnetic moments for various compositions of $Mg_{0.25-x}Ni_xCu_{0.25}\ Zn_{0.5}\ Fe_2O_4$ ferrites. The experimental magnetic moment was increased with increase in Ni content whereas the α_{y-k} was decreased. The decrease in α_{y-k} is mainly due to substitution of Ni having high magnetic moment than for Mg with zero magnetic moment

3.5.3 Initial permeability

The room temperature initial permeability (μ_i) of synthesized ferrites was measured in the frequency range of 100 kHz–10 MHz. The μ_i value of the ferrites exhibited a constant behavior up to a certain frequency and then-after increased with further increase in the frequency (Fig. 7a). In case of Ni doping, μ_i value increased with Ni content $x = 0.05$ and then decreased with further increase in Ni. The said variations are due to different sintering density.

Initial permeability at ambient temperature (μ_i) and during temperature cycle ($\Delta\mu_i$) is tabulated below in Table 3. The ferrites with higher densities exhibited high μi value. It was observed that for Ni doping greater than $x = 0.05$, μ_i decreases. This reduction is due to an increase in magnetostriction constant by substitution of Ni to Mg. The rotational (μ_{rk}) and wall (μ_w) permeability were also calculated

Table 3 Data on magnetic parameters like saturation magnetization (M_s), M_r/M_s, coercivity (H_c), initial permeability (μ_i), rotational permeability (μ_{rk}), wall permeability (μ_w), magneto crystalline anisotropy constant (K_1), thermal hysteresis of initial permeability, Curie temperature (T_C) from $\chi_{a.c}$ and μ_i for all the ferrites

#	Content of Ni (x)	M_s (emu)	M_r/M_s	H_c	μ_i	μ_{rk}	μ_w	μ_{ih}	μ_{ic}	$\Delta\mu_i$	$K_1 \times 10^4$ (erg/cc)	T_C (°C) from χ_{AC}	T_C (°C) from μ_i
1	0.00	239	0.0038	3.41	1268	17	1252	1400	1500	100	−2.50	145	140
2	0.05	263	0.0029	2.73	2620	14	2607	3100	3198	98	−2.63	158	149
3	0.10	290	0.0034	3.27	1930	19	1912	2500	2567	67	−2.77	182	170
4	0.15	248	0.0041	4.06	1569	13	1557	1900	2050	50	−2.90	200	190
5	0.20	341	0.0050	4.79	522	24	499	512	557	45	−3.04	212	210
6	0.25	318	0.0049	5.06	520	20	501	600	636	36	−3.17	226	231

Table 4 The probable cation distribution and the magnetic moments of all the ferrites

#	x	Cation distribution	n_B Th.	n_B Expt.	α_{y-k}
1	0.00	$(Mg_{0.025}Cu_{0.025}Zn_{0.5}Fe_{0.45})^A\ [Mg_{0.225}Cu_{0.225}Fe_{1.55}]^BO_4$	5.999	1.94	59°16′12″
2	0.05	$(Mg_{0.020}Cu_{0.020}Zn_{0.5}Fe_{0.46})^A\ [Ni_{0.05}Mg_{0.180}Cu_{0.230}Fe_{1.54}]^BO_4$	5.964	2.15	58°51′52″
3	0.10	$(Mg_{0.015}Cu_{0.015}Zn_{0.5}Fe_{0.47})^A\ [Ni_{0.10}Mg_{0.135}Cu_{0.235}Fe_{1.53}]^BO_4$	5.948	2.32	55°37′24″
4	0.15	$(Mg_{0.010}Cu_{0.010}Zn_{0.5}Fe_{0.48})^A\ [Ni_{0.15}Mg_{0.090}Cu_{0.240}Fe_{1.52}]^BO_4$	5.932	2.10	57°23′2″
5	0.20	$(Mg_{0.005}Cu_{0.005}Zn_{0.5}Fe_{0.49})^A\ [Ni_{0.20}Mg_{0.045}Cu_{0.245}Fe_{1.51}]^BO_4$	5.916	2.70	51°57′55″
6	0.25	$(Cu_{0.0025}Zn_{0.5}Fe_{0.4975})^A\ [Ni_{0.25}Cu_{0.2475}Fe_{1.5025}]^BO_4$	5.918	2.52	53°23′35″

using the following formulae:

$$\mu_{rk} = 1 + 2\pi M^2 s/lk_1, \tag{5}$$

$$\mu_w = \mu_i - (\mu_{rk} - 1) \tag{6}$$

The magnitude of μ_w was found relatively larger in comparison with μ_{rk}, for all compositions of $Mg_{0.25-x}Ni_xCu_{0.25}Zn_{0.5}Fe_2O_4$ ferrite. Thus, a conclusion can be drawn that the main contribution to the initial permeability is due to domain wall motion. The value of initial permeability at $x = 0.05$ is almost twofold greater than at $x = 0.00$ (Mg–Cu–Zn ferrite) and fivefold greater than $x = 0.25$ (Ni–Cu–Zn ferrite). The high value of initial permeability exhibited by sample with $x = 0.05$ is mainly attributed to the higher sintered density and higher grain size exhibited by that sample.

Figure 7b shows the variation of initial permeability as a function of temperature for different compositions of ferrites. The initial permeability exhibited a constant behavior up to a particular temperature then achieves a peak value and then suddenly drops to a minimum value at Curie temperature. The abrupt decrease in initial permeability at Curie temperature is the sign of transition from ferrimagnetic state to the paramagnetic state, as discussed above. Furthermore, the magnitude of Curie temperature increased with an addition of Ni^{2+}, which is mainly due to the magnetic nature of Ni^{2+} than nonmagnetic nature of Mg^{2+} at octahedral site. The variation of magnetic loss factor with temperature is shown in Fig. 7c. Higher the value of initial permeability, lower is the value of loss factor. As the initial permeability drops to a minimum value at Curie temperature, the loss factor got increased at higher temperature scale. The ferrite with $x = 0.05$ exhibited lowest value of loss factor at room temperature, indicating its suitability for MLCI applications.

4 Conclusions

In conclusion, we developed a simple and straight forward synthesis strategy for fabricating spinel-type Ni^{2+}-substituted Mg–Cu–Zn nanocrystalline ferrite through citrate gel combustion process. The doping level of Ni is varied in the range of $0 \le x \le 0.25$, where the system is $Mg_{0.25-x}Ni_xCu_{0.25}Zn_{0.5}Fe_2O_4$. Citrate gel method yielded a single-phase ferrite material with high density and dense microstructure. The structural, morphological, transport, dielectric, and magnetic properties of the ferrites are discussed. The microstructure was strongly influenced by the addition of Ni^{2+}. The addition of nickel results in increased aggregation of the colloidal backbone of ferrite and the loss of the mesoporous network structure. The DC resistivity study confirmed the semiconducting nature of the material and ferrite samples exhibited high resistivity values making them useful for high frequency applications. The electric transport, dielectric, and magnetic properties were strongly found to be dependent on Ni content. With increasing Ni content, an increase in the activation energy (upto $x = 0.10$), decrease in loss tangent and saturation magnetization, are observed. Magnetic properties reveal that the $Mg_{0.25-x}Ni_xCu_{0.25}Zn_{0.5}Fe_2O_4$ with $x = 0.05$, due to its lowest coercivity

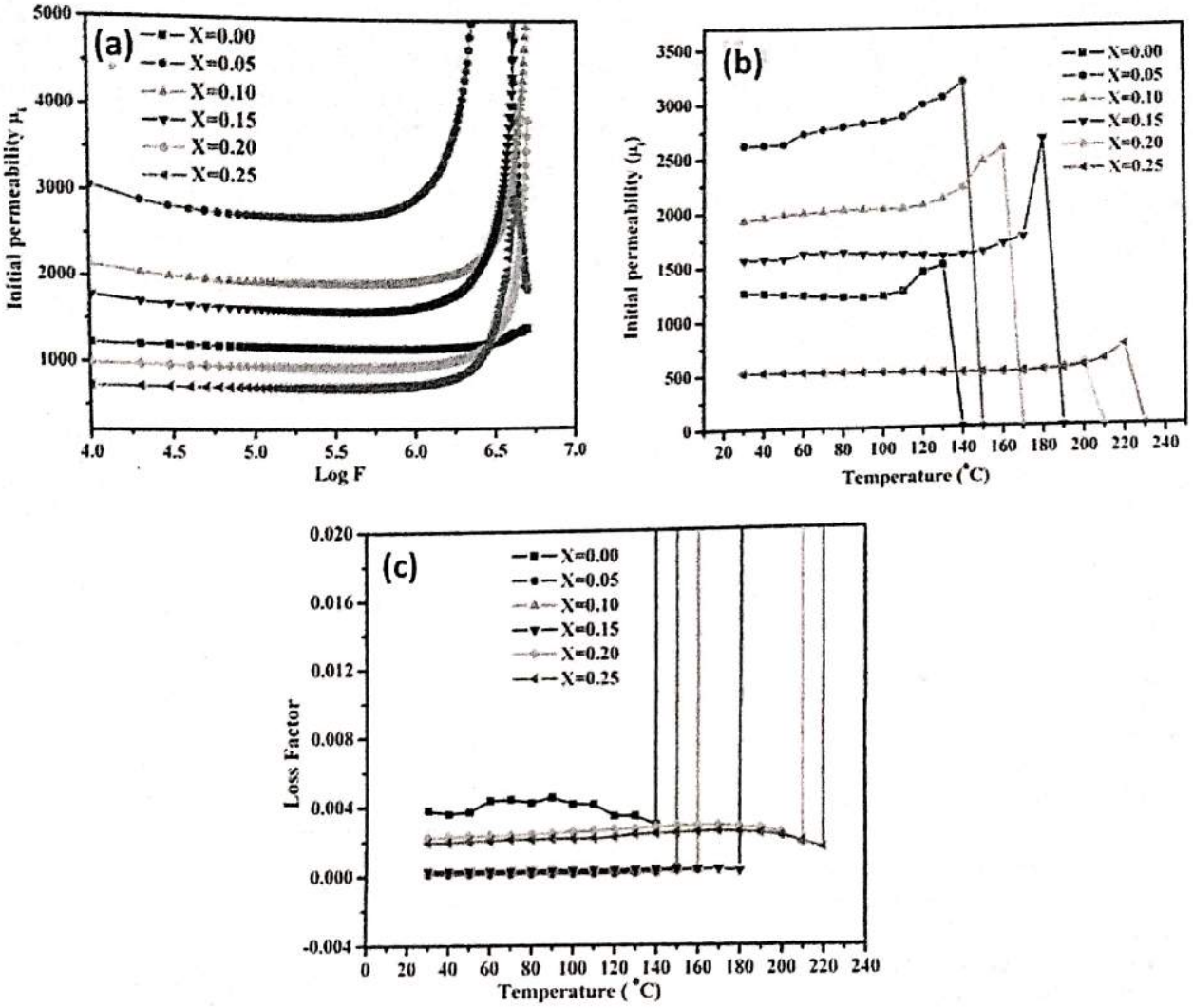

Fig. 7 Permeability studies of the ferrites. a Frequency dependency of initial permeability (μ_i), b, c temperature dependency of permeability and loss factor

and highest initial permeability, would be the suitable material in MLCI with reduced layers and more miniaturization.

Acknowledgements RCK thankfully acknowledges the Indian Space Research Organization (ISRO-UoP) Space Technology Cell, Government of India (Grant No. GOI-A-337 (B) (137)), and BCUD, Savitribai Phule Pune University (Grant No. RG-31) for providing research funding.

Compliance with ethical standards

Conflict of interest The authors declare that they have no conflict of interest.

References

1. Sutka A, Grossa KA (2016) Spinel ferrite oxide semiconductor gas sensors. Sens Actuators B 222:95–105
2. Valenzuela R (2012) Novel applications of ferrites. Phys Res Int 2012: 591839. https://doi.org/10.1155/2012/591839
3. Subramani A, Kondo K, Tada M, Abe M, Yoshimura M, Matsushita N (2009) High resistive ferrite films by a solution process for electromagnetic compatible (EMC) devices. J Mag Mag Mat 321:3979–3983
4. Adam JD, Davis LE, Dionne GF, Schloemann EF, Stitzer SN (2002) Ferrite devices and materials. IEEE Trans Microw Theory Tech 50:721–737
5. Pique A, Chrisey DB (2002) Direct-write technologies for rapid prototyping applications: sensors, electronics and integrated power sources. Academic Press, New York, USA
6. Rao P, Godbole RV, Bhagwat S (2016) Copper doped nickel ferrite nano-crystalline thin films: a potential gas sensor towards reducing gases. Mater Chem Phys 171:260–266
7. Akhtar MN, Khan MA, Mukhtar A, Nazir MS, Imran M, Ali A, Sattar A, Murtaza G (2017) Evaluation of structural, morphological and magnetic properties of CuZnNi ($Cu_xZn_{0.5-x}Ni_{0.5}Fe_2O_4$) nanocrystalline ferrites for core, switching and MLCIas applications. J Mag Mag Mat 421:260–268

8. Sharma R, Thakur P, Sharma P, Sharma V (2017) Ferrimagnetic Ni^{2+} doped Mg-Zn spinel ferrite nanoparticles for high density information storage J Alloy Comp 704:7–17
9. Hoque SM, Huang Y, Cocco E, Maritim S, Santin AD, Shapiro EM, Coman D, Hyder F (2016) Improved specific loss power on cancer cells by hyperthermia and MRI contrast of hydrophilic $Fe_xCo_{1-x}Fe_2O_4$ nanoensembles Contrast Media Mol Imaging 11:514–526
10. Roy PK, Bera J (2012) Study on electromagnetic properties of MgCuZn ferrite/$BaTiO_3$ composites. Mater Chem Phys 132:354–357
11. Penchal Reddy M, Madhuri W, Venkata Ramana M, Ramamanohar Reddy N, Siva Kumar KV, Murthy VRK, Siva Kumar K, Ramakrishna Reddy R (2010) Effect of sintering temperature on structural and magnetic properties of NiCuZn and MgCuZn ferrites. J Magn Magn Mater 322:2819–2823
12. Ch. Sujatha K, Venugopal Reddy K, Sowri B, Rama Chandra Reddy A, Rao KH (2013) Effect of sintering temperature on electromagnetic properties of NiCuZn ferrite. Ceram Int 39:3077–3086
13. Trukhanov SV, Trukhanov AV, Kostishin VG, Panina LV, Kazakevich IS, Turchenko VA, Kochervinskiy VV (2016) Coexistence of spontaneous polarization and magnetization in substituted M-type hexaferrites $BaFe_{12-x}Al_xO19$ ($x \leq 1.2$) at room temperature. JETP Lett 103:100–105
14. Trukhanov AV, Trukhanov SV, Panina LV, Kostishyn VG, Chitanov DN, Kazakevich IS, Trukhanov AV, Turchenko VA, Salem M (2017) Strong corelation between magnetic and electrical subsystems in diamagnetically substituted hexaferrites ceramics. Ceram Int 43:5635–5641
15. Hameed AS, Bahiraei H, Reddy MV, Shoushtari MZ, Vittal JJ, Ong CK, Chowdari BVR (2014) Lithium storage properties of pristine and (Mg, Cu) codoped $ZnFe_2O_4$ nanoparticles ACS Appl Mater Interfaces 6:10744–10753
16. Afkhami A, Bahiraei A, Madrakian T (2017) Application of nickel zinc ferrite/graphene nanocomposite as a modifier for fabrication of a sensitive electrochemical sensor for determination of omeprazole in real samples. J Colloid Interface Sci 495:1–8
17. Satalkar M, Kane SN, Kumaresavanji M, Araujo JP (2017) On the role of cationic distribution in determining magnetic properties of $Zn_{0.7-x}Ni_xMg_{0.2}Cu_{0.1}Fe_2O_4$ nano ferrite. Mater Res Bull 91:14. https://doi.org/10.1016/j.materresbull.2017.03.021
18. Barati MR (2009) Characterization and preparation of nanocrystalline MgCuZn ferrite powders synthesized by sol–gel autocombustion method. J Sol-Gel Sci Technol 52:171–178
19. Li J, Wang X, Song K, Li Q, Gong R, Su Z, Chen Y, Harris VG (2015) High magnetic loss Mg–Cu ferrites for ultrahigh frequency EMI suppression applications. IEEE Trans Magn 51:1. https://doi.org/10.1109/TMAG.2015.2428718
20. Gabal MA, Angari YMAl (2010) Low-temperature synthesis of nanocrystalline NiCuZn ferrite and the effect of Cr substitution on its electrical properties. J Magn Magn Mater 322:3159
21. Sujatha C, Venugopal Reddy K, SowriBabu K, Ramachandra Reddy A, Rao KH (2012) Structural and magnetic properties of Mg substituted NiCuZn nano ferrites. Phys B 407:1232–1237
22. Bhosale DN, Verenkar VMS, Rane KS, Bakare PP, Sawant SR (1999) Initial Susceptibility Studies on Cu-Mg-Zn Ferrites. Mater Chem Phys 59:57–62
23. Weast RC (ed) (1972) CRC handbook of chemistry and physics, 53rd edn. CRC Press, Boca Raton, p. D-120
24. Zayat M, Levy D (2000) Blue CoAl2O4 Particles prepared by the sol-gel and citrate-gel methods. Chem Mater 12:2763–2769
25. Bhosale DN, Choudhari ND, Sawant SR, Bakare PP (1997) Initial permeability studies on high density Cu-Mg-Zn ferrites. J Magn Magn Mater 173:51–58
26. Barati MR (2009) Influence of zinc substitution on magnetic and electrical properties of MgCuZn ferrite nanocrystalline powders. J Alloy Compd 478:375–380
27. Ahmed Farag IS, Ahmed MA, Hanmad SM, Moustafa AM (2001) Study of cation distribution in $Cu_{0.7}(Zn_{0.3-x}\ Mg_x)Fe_{1.7}Al_{0.3}O_4$ by X-ray diffraction using Rietveld method Egypt J Solids 24:215–226
28. Gupta TK, Coble RL (1968) Sintering of ZnO: I, densification and grain growth. J Am Ceram Soc 51:521–525
29. Su H, Zhang H, Tang X, Lu B, Zhong Z (2009) Study on low-temperature sintered NiCuZn and MgCuZn spinel ferrites. J Alloy Compd 475:683–685
30. Reddy MP, Kim IG, Yoo DS, Madhuri W, Venkata Ramana M, Shaaban A, Reddy NR, Siva Kumar KV, Reddy RR (2013) Effect of La substitution on structural and magnetic properties of microwave treated $Mg_{0.35}\ Cu_{0.05}\ Zn_{0.60}\ La_xFe_{2-x}O_4$ ceramics. Superlattices Microstruct 56:99–106
31. Reddy MP, Mohamed AM (2015) One-pot solvothermal synthesis and performance of mesoporous magnetic ferrite MFe_2O_4 nanospheres Microporous Mesoporous Mater 215:37–45
32. Low KO, Sale FR (2002) Electromagnetic properties of gel-derived NiCuZn ferrites. J Magn Magn Mater 246:30–35
33. Bellad SS, Watawe SC, Chougule BK (1999) Microstructure and permeability studies of mixed Li-Cd ferrites. J Magn Magn Mater 195:57–64
34. Su H, Tang X, Zhang H, Zhong Z, Shen J (2011) Sintering dense NiZn ferrite by two-step sintering process. J Appl Phys 109:07A501
35. Venugopal Reddy P, Seshagiri Rao T, Rao SMD (1981) Electrical conductivity of lithium-nickel ferrites. J Less Common Met 79:191–198
36. Koops CG (1951) On the dispersion of resistivity and dielectric constant of some semiconductors at audio frequencies. Phys Rev 83:121–124
37. Ahmed MA, Bishay ST (2004) The magnetic and electrical properties of Cr^{3+} substituted nickel ferrite J Magn Magn Mater 279:178
38. Ahmed MA, Mansour SF, El-Dek SI, Ahmed MA, Mansour SF, El-Dek SI (2010) Investigation of the physico-chemical properties of nanometric NiLa ferrite/PST matrix. Solid State Ion 181:1149–1155
39. Su H, Zhang H, Tang X (2006) Effects of calcining temperature and heating rate on properties of high-permeability NiCuZn ferrites. J Magn Magn Mater 302:278–281